Three-dimensional holographic optical manipulation through a high-numerical-aperture soft-glass multimode fibre

Leite, Ivo T.; Turtaev, Sergey; Jiang, Xin; Šiler, Martin; Cuschieri, Alfred; Russell, Philip St J.

Published in:
Nature Photonics

DOI:
10.1038/s41566-017-0053-8

Publication date:
2018

Document Version
Peer reviewed version

Submitted 15th June 2017, Revised 31st August 2017
Research article

3-D holographic optical manipulation through high-NA soft-glass multimode fibre

Ivo T. Leite[1,2,3], Sergey Turtaev[1,4], Xin Jiang[5], Martin Šiler[6], Alfred Cuschieri[2], Philip St.J. Russell[5], and Tomáš Čižmár[1,6*]

Abstract

Holographic optical tweezers (HOT) holds great promise for many applications in modern biophotonics, allowing the creation and measurement of minuscule forces on biomolecules, molecular motors and cells. Optical geometries used in HOT currently make use of bulk optics, and their usage *in-vivo* is compromised by the optically turbid nature of living tissues – a limiting factor in any advanced high-resolution imaging method. We present an alternative HOT approach in which multiple three-dimensional optical traps are introduced through a high-numerical-aperture multimode optical fibre, thus enabling an equally versatile means of optical manipulation through channels having cross-section comparable to the size of a single cell. Our work demonstrates real-time manipulation of 3-D arrangements of micro-objects, as well as the possibility of manipulating inside otherwise inaccessible cavities. We show that the position of the optical traps can be controlled with nanometric resolution over fibre lengths exceeding 100 mm. The results provide the basis for exploitation of holographic manipulation and other high-numerical-aperture techniques, including advanced forms of microscopy, through single-core-fibre endoscopes deep inside living tissues and other complex environments.

Subject terms
Fibre optics, Adaptive optics, Optical manipulation, Optical tweezers

[1] *SUPA, School of Science and Engineering, University of Dundee, Nethergate, Dundee DD1 4HN, Scotland, United Kingdom*
[2] *Institute of Medical Science and Technology, University of Dundee, Dundee Medipark, Dundee DD2 1FD, Scotland, United Kingdom*
[3] *Leibniz Institute of Photonic Technology, Albert-Einstein-Straße 9, 07745 Jena, Germany*
[4] *School of Life Sciences, University of Dundee, Nethergate, Dundee DD1 4HN, Scotland, United Kingdom*
[5] *Max Planck Institute for the Science of Light, Staudtstraße 2, 91085 Erlangen, Germany*
[6] *Institute of Scientific Instruments of the CAS, Královopolská 147, 612 64 Brno, Czech Republic*
*__Corresponding author__: t.cizmar@dundee.ac.uk

Optical tweezers, a tightly focussed laser beam, allows for stable contactless three-dimensional confinement and manipulation of micro- and nano-objects [1]. Many exciting applications of this concept have been demonstrated across the domain of biophysics, particularly due to their ability to precisely exert and measure sub-piconewton forces on single molecules or molecular assays [2]. To date, optical tweezers have made many contributions to our understanding of molecular motors and the functionality of biological polymers driving the mechanics of cells [3–5]. Holographic optical tweezers (HOT) represent the most advanced optical manipulation technique that through the use of wavefront shaping facilitates a multitude of trapping sites which can be simultaneously manoeuvred in all three dimensions at will [6–8]. HOT share numerous similarities with the methods of modern microscopy [9–12], including instrumentation, particularly the reliance on high numerical aperture (NA) objective lenses as well as the difficulty in reaching higher penetration depths in optically turbid tissues. There is a great desire to study the mechanics of biological processes directly within the complexity of living organisms and at present the practical applications can only reach few tens of micrometres [13–15]. A perspective strategy to overcome the turbid nature of scattering tissues is the employment of optical fibres, minimally invasive light-guides providing optical access inside. Fibre-based manipulation schemes date back to the early 1990s [16]. Static three-dimensional optical traps have been constructed using single-mode fibres in combination with elaborate terminations [17–19]. The first systems capable of one-dimensional manipulation were realised in counter-propagating dual-fibre schemes [20, 21], and later, by exploitation of few-mode fibres, enabled the controlled rotation of cells [22, 23].

Parallel efforts to break through the turbidity barrier have efficiently utilised the deterministic propagation of coherent light through turbulence, based on a feedback of light intensity from within a given medium [24–26]. This has also resulted in the demonstration of optical manipulation through turbid layers [27], a concept which however is not directly implementable *in-vivo*, since optical feedback from within a living tissue is not readily available. Nonetheless, these strategies became recently very relevant in the context of

manipulation through optical fibres: Wavefront-shaping technology applied to control the light propagation through multimode fibres (MMF), can turn such fibres into ultra-narrow, minimally invasive endoscopes [28–38]. Light transmission through MMFs is a complex, seemingly chaotic process. Coherent optical fields propagating in MMFs acquire apparently random phase relations resulting in speckle output patterns bearing no resemblance to the incident fields. In this context, wavefront shaping has arisen as a powerful tool for controlling this complex behaviour. It has allowed the engineering of various elaborate beam shapes including laser foci precisely positioned across the fibre output facet [28, 29], and subsequently the reconstruction of images from the light signals reflected backwards along the fibre [30–32, 39]. These studies also brought the possibility of two-dimensional (lateral) optical manipulation [29, 30]. Due to the limited NA of the commercially available MMFs, however, the resulting foci could not provide full three-dimensional capture of micro-objects. Confined particles therefore had to be prevented from escaping the optical traps along the optical axis, which was realised by trapping against a sample boundary (coverslip).

Three-dimensional confinement typically requires a very high NA (typically around 1). There are several approaches available to enhance the NA of MMFs. These include photonic crystal fibres, offering NAs of up to 0.61 [38]. While this value can be further enhanced to meet the requirements for stable confinement, these fibres may not be suitable for manipulation in practice, since changes to light propagation induced by liquids entering the hollow fibre channels render such fibres unsuitable for use in aqueous environments. The NA of standard MMFs can also be enhanced by means of alternative terminations. Introducing highly turbid layers to the distal facet facilitates NA enhancement to the levels suitable for optical manipulation [39, 40]. The output modes in this case significantly outnumber the input modes, which poses limits to the control of output fields, resulting in strong random background signals interfering with the foci. Alternative carefully engineered terminations [41] do not suffer from this issue but the price to pay is in the extended footprint of the instrument.

Taking these trade-offs into account we conclude that the ideal candidate for *in vivo* optical manipulation would be all-solid, step-index MMF with a very high contrast of refractive indices between the fibre core and the cladding thus yielding a very-high NA. Therefore we have designed and manufactured such MMF based on compound "soft-glasses" with an overall diameter as small as 35 µm, offering a uniform high NA across the entire fibre core, which exceeds the value needed for stable 3-D confinement of silica microparticles in water (see Supplementary Results 2 for details of the minimum NA needed). Implementing methods of holographic control of light through the fibres we have encountered a new challenge inherent in such high-NA fibres - a very strong mode-dependent power loss (MDL). This has necessitated the development of new instrumentation and holographic approaches to take the MDL into account, which enabled us to harness the available NA almost completely, and in result, successfully implement 3-D HOT. We have shown the possibility of manipulating multiple objects in elaborate predefined arrangements and demonstrated its functionality inside an optically turbid cavity, thus clearly demonstrating that the technique is suitable for use in complex, hard-to-access environments, including living tissues. Finally, we have analysed the performance of the system in a series of quantitative measurements of trap stiffness for different fibre lengths, and of the positioning accuracy of the confined objects.

Fibre design and fabrication

For the purposes of all studies in this Article, as well as other applications requiring high-NA focussing, we have developed a novel soft-glass step-index multimode fibre. Two lead-silicate glasses with very different refractive indices are used as the core and cladding materials (respectively, Schott SF57: a dense flint glass, with refractive index 1.8117 at 1064 nm, and Schott LLF1: a very light flint, with refractive index 1.5346 at 1064 nm). Such high refractive index contrast yields an NA exceeding 1 at wavelengths below 620 nm and 0.96 at 1064 nm – values previously only accessible using photonic crystal fibres [42]. The fibre features a core diameter of 20 µm and at 1064 nm supports approximately 1600 guided modes.

To demonstrate their potential as minimally-invasive probes, the fibre end was post-processed into a flat-cone termination as shown in Supplementary Figure S9. Further information concerning the fabrication and post-processing of the fibres is available in the Methods section.

High-resolution focussing and mode-dependent loss

The propagation of light through MMFs is a deterministic and linear process, and so can be represented as a superposition of a set of preferentially orthogonal modes and modelled using a complex-valued transmission matrix (TM) [43, 44]. The optimal choice of modal set depends on the particular application. Since optical traps are essentially tightly focussed laser beams, in our case the TM is empirically measured in the representation of diffraction-limited focal points (FPs), organised across an orthogonal grid [35]. Following this calibration step, we can invert the measured TM and readily design a holographic modulation of the light which, upon implementation using a spatial light modulator, forms FP-generating fields at the proximal end of the fibre. These proximal fields, after being launched into the MMF, result in a single FP mode, or an arbitrary composition of FPs located at desired positions across the fibre output facet.

Unlike other complex media, however, MMFs have axially-invariant cylindrical symmetry, which as explained below, can be efficiently utilised to achieve axial positioning of output FPs as well as the manipulation of their spatial content.

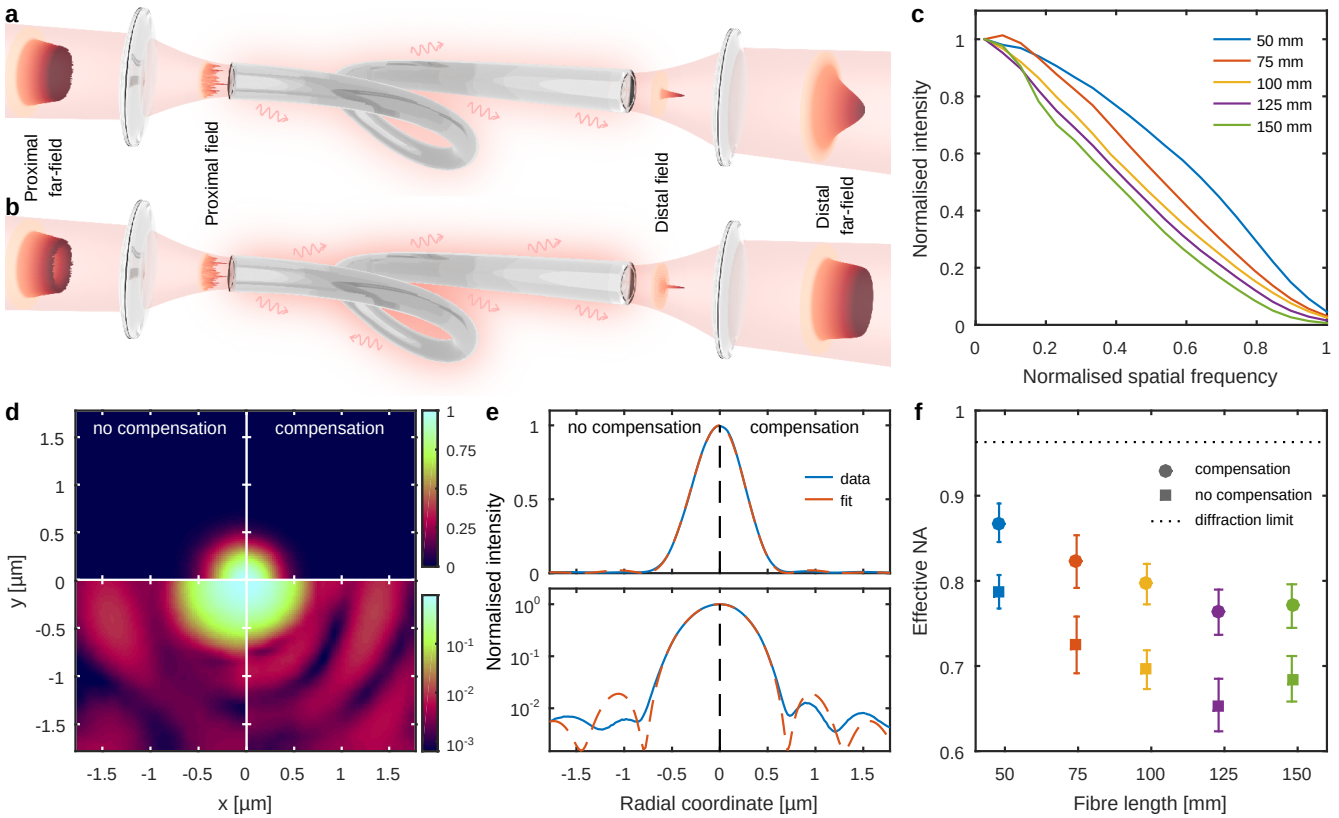

Figure 1. High-resolution focussing through a multimode fibre. **a**, The presence of mode-dependent loss (MDL) in multimode fibres preferentially attenuates the higher transverse spatial frequencies, i.e. lower propagation constants. **b**, MDL can be pre-compensated in the proximal far-field so as to equalise the power spectrum in the distal far-field. **c**, Azimuthally averaged intensity distribution at the distal far-field (prior to the MDL compensation), showing the influence of MDL for different fibre lengths. **d**, Intensity profile of a distal focal point (FP) with and without MDL-compensation. **e**, Azimuthally averaged intensity profile of the distal FP, with a fit to the expected Airy disk distribution. **f**, Effective NA of FPs generated at 91 different positions across the distal fibre endface, with and without MDL compensation, for varying fibre lengths.

The cylindrical symmetry gives the origin of mutually orthogonal propagation-invariant modes, also called eigenmodes [35, 45], that maintain their transverse field distributions during propagation. In highly multimode fibres, the propagation-invariant modes can be grouped into families with similar propagation constants that do not exchange power. Even in deformed fibres, intermodal coupling occurs predominantly within each mode-group, not between mode-groups, which preserves the identity of each mode-group during propagation. In step-index MMFs, as shown in [31], each mode-group occupies a different annular zone in the proximal far-field and due to the propagation invariance and lack of coupling it will also be found at the same annular zone at the distal far-field after leaving the fibre. In order to utilise this feature to manipulate distal FP modes, let us mention that shifting a focus axially can generally be achieved by adding a defocus – a positive or negative quadratic phase term – to its far-field. Since such modulation is completely azimuthally independent, its application to the proximal far-field will result in the same change to the distal far-field. This way the distal FP modes can conveniently be repositioned in the axial direction simply by adding the defocus to the proximal far-field, thus eliminating the necessity of performing multiple TM acquisitions for different axial distances behind the fibre.

The same feature also makes it possible to normalise the power – a vitally important matter due to significant mode-dependent loss (MDL) in these new fibres. In any MMF, individual mode-groups experience different amounts of attenuation [46, 47], those with smaller propagation constants (with higher transverse spatial frequencies) having higher loss (Fig. 1a). In previous studies with commercially available low-NA MMFs, this effect did not become apparent. In the new high-NA fibres over lengths of a few centimetres, however, we have observed a substantial difference in the attenuation of different mode-groups, exceeding one order of magnitude, as shown in Fig. 1c. The resulting non-uniformity of the distal far-field thus impairs full exploitation of the available NA. In order to tackle this limitation, it is therefore necessary to significantly intensify the higher-order mode-groups in order to achieve the uniform distal far-field distribution, as depicted in Fig. 1b. In the conventional HOT approach the spatial light modulator is relayed onto the back focal plane of the coupling

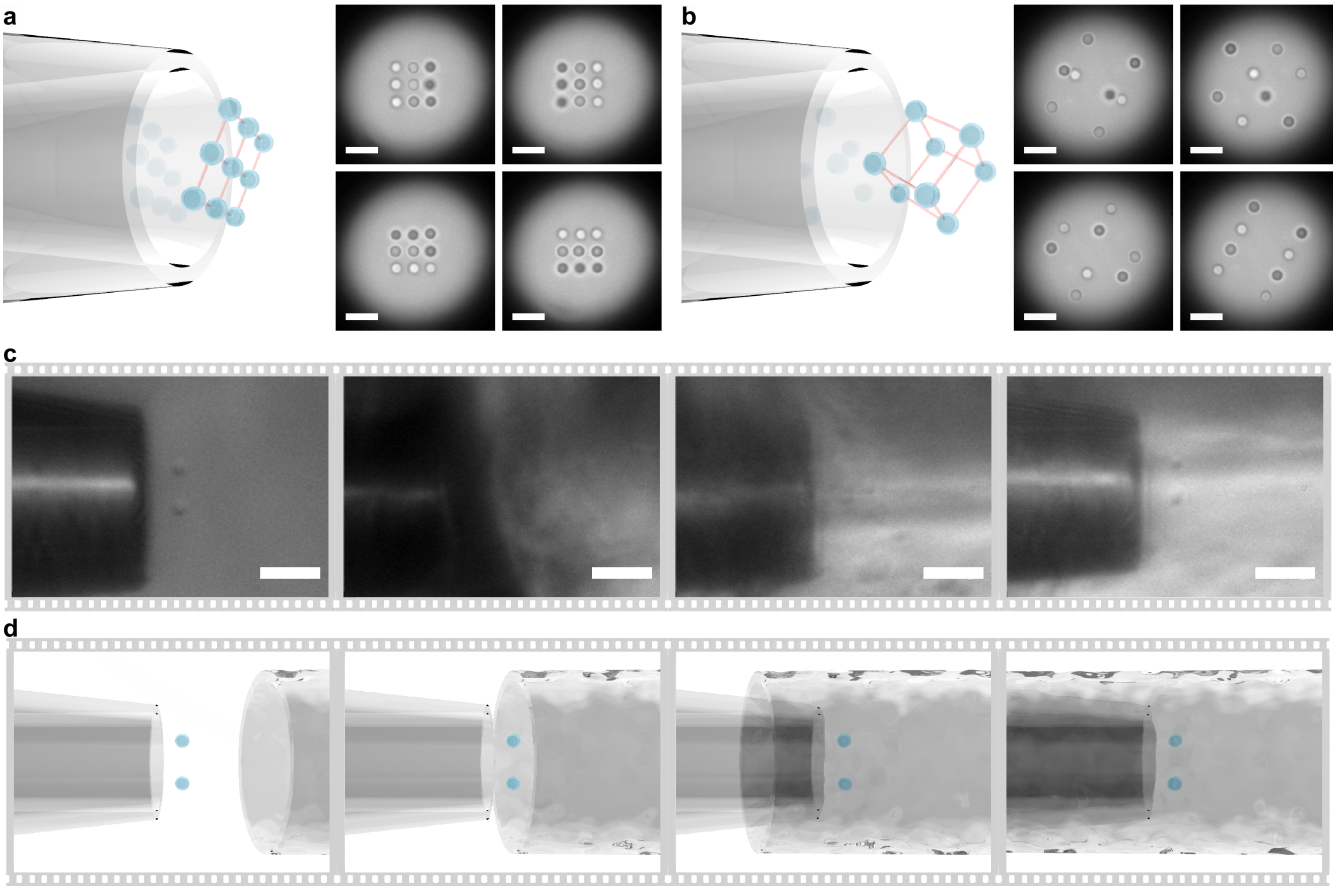

Figure 2. Multiple holographic tweezers delivered through a lensless multimode fibre. a,b, Multiple holographic tweezers trapping of **(a)** nine particles in a square-grid arrangement, and **(b)** eight particles forming a rotating three-dimensional cube. The different brightness of the particles arises from their varying axial positions relative to the focal plane of the imaging microscope objective (the particles appearing 'brighter' are at a greater distance from the fibre endface). Incoherent light for illumination is also delivered through the fibre core, which is visible as a blurred disk in the background. The scale-bars correspond to 5 µm. **c,d,** Optical manipulation of two particles inside a turbid cavity comprising a complex, hard-to-access environment. The scale-bars correspond to 10 µm. In **(a-d)**, all the particles are 1.5 µm-diameter silica microspheres in a water suspension, the fibre length is 65 mm, and the *in vacuo* trapping wavelength is 1064 nm.

objective, i.e. a plane conjugate to the proximal far-field. The only way to achieve the required power distribution in this arrangement is to discard the excessive power in the central zones, which would be associated with a significant power loss. Therefore we have modified the system in order to project the spatial light modulator onto the fibre facet, as by altering the spatial content of the holographic modulation in this arrangement, we can redistribute the power at will between the central and the peripheral zones of the proximal far-field without incurring such prohibiting power loss. In Fig. 1d,e the same distal FP mode is compared before and after MDL compensation, indicating an NA enhancement of ≈ 0.1. As seen in Fig. 1f, this value is well maintained for different lengths of the fibre (see Supplementary Results 3 for further details). Even after the MDL compensation, the decreasing trend of NA as a function of the fibre length persists. We speculate that the decreasing signal strength of the higher order modes is associated with growing levels of noise during the TM acquisition, which further affects the higher spatial frequencies of the generated output foci thus limiting their NA.

Multi-trap and 3-D manipulation in complex environments

The high beam quality after MDL compensation allowed us to demonstrate three-dimensional optical trapping with bare multimode fibres up to 150 mm long. The geometry used in these experiments is detailed in the Supplementary Methods 1. The technique allowed both simultaneous generation of multiple trap sites and independent control of their position in all three dimensions. Figure 2a shows the *en face* view of nine silica particles trapped in a square-grid arrangement in front of the fibre endface. Incoherent light for illumination is delivered to the scene also by the fibre core and is visible as a blurred bright disk in the background. In Fig. 2b the three-dimensional

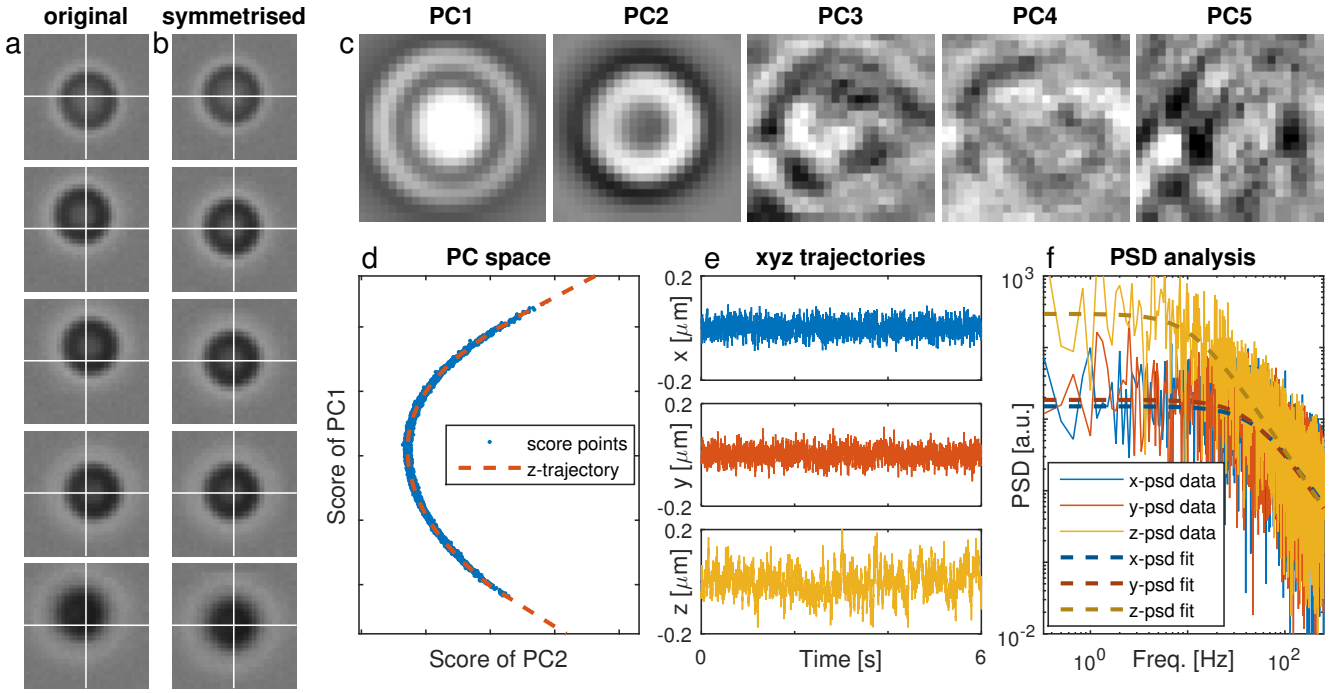

Figure 3. Particle tracking based on symmetry and principal component analysis. a, Sequence of original CCD frames. **b,** Symmetrised frames of **(a)**. **c,** The first five principal components of the symmetrised record. **d,** Z-coordinate trace in the space of the score of the two principal components. **e,** Retrieved time-evolution of all three Cartesian coordinates of the trapped particle. **f,** Power spectrum density and its Lorentzian fit for each coordinate.

dynamic control of the optical tweezers is demonstrated by trapping eight particles simultaneously in a rotating cube arrangement. The images show snapshots of a video recording of the rotating structure (full video is available as Supplementary Media SM1). The available volume within which the NA is high enough to ensure stable 3-D confinement is indicated in the Supplementary Results 1.

With such a small footprint, the fibre-based HOT could now allow access to optically inaccessible cavities. To verify this, we prepared a small semi-opaque tube of roughly polished of PMMA with an open channel ∼125 µm wide. An additional optical pathway was set up to allow imaging of the sample from the side. Side-views of simultaneous optical tweezing of two particles, recorded while the fibre was inserted into the tube, are shown in Fig. 2c,d (see also Supplementary Media SM4).

Characterisation of the optical tweezers

In aqueous media, confined particles are subject to Brownian motion so that recording their 3-D trajectories can be used to analyse the strength (stiffness) of the optical trap. Since fibre-based HOT is incompatible with the standard approach of back-focal-plane interferometry [48], we developed an algorithm to extract the particle positions from high-speed video recordings. The particles used are highly regular spheres, so that their images produce azimuthally invariant signals over a uniform background (see Fig. 3a). As a first step, we employ the shift-property of the Fourier transform to translate the particle image to the centre of the frame, so the whole frame features the best horizontal and vertical symmetries (Fig. 3b). The shift-property of the Fourier transform is very suitable for this operation as even for non-integer pixel shifts it does not affect the spatial content of the images (see Methods for the mathematical background). The amount of particle image shift immediately yields the lateral x and y trajectories, which can be calibrated using the known magnification of the imaging system. This procedure also provides a stack of symmetrised video-frames where the shape of the particle image changes only with axial position (z). As there is only one degree of freedom dictating the changes in the particle image shape, the z coordinate can be extracted using principal component analysis, a multivariate algorithm commonly used to reduce the dimensionality of datasets. Changes to signals of individual pixels in symmetrised frames are, due to the axial motion of the particle, correlated. Principal component analysis transforms this multidimensional space of pixel signals into a set of orthogonal vectors (principal components) in a way that the first principal component would contain the maximum variance of the data set, the second principal component would contain the next most significant variance and so on. As shown in Fig. 3c, only the first two principal components (PC1 and PC2) feature azimuthal symmetry and are not overwhelmed by noise; therefore, we can assume that these variances carry most of the

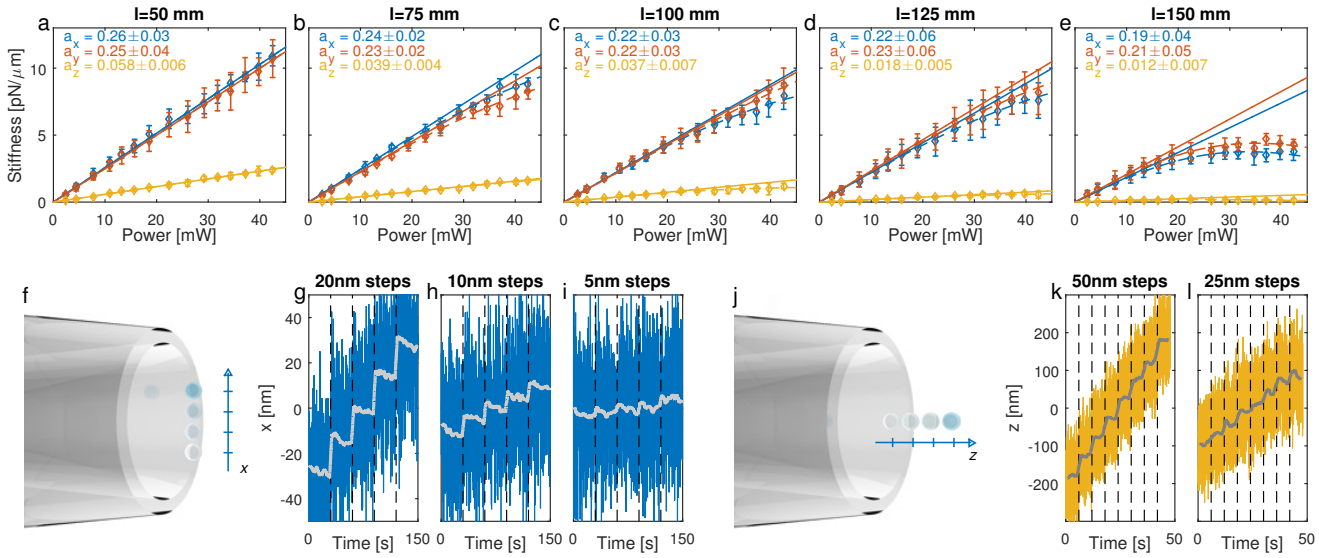

Figure 4. Performance of multimode fibre based holographic tweezers. a-e, Trap stiffness for each coordinate as a function of the total optical power leaving the distal fibre end, for various fibre lengths. Since the dependence visibly deviates from linearity, the data-set has been fitted to $\kappa = aP\exp(-\frac{P^2}{b^2})$ (dashed lines), where κ is the stiffness, P is the output optical power, and a and b are two fitting parameters. The parameter a reveals the initial linear trend (solid lines) and its calculated found values (in units of pN/μm/mW) are included in the top-left corner of each plot. **f-i,** Sequential relocation of the trap site along the lateral direction in increments of (**g**) 20 nm, (**h**) 10 nm, and (**i**) 5 nm . **j-l,** Sequential relocation of the trap site along the axial direction in increments of (**k**) 50 nm and (**l**) 25 nm.

information about the particle's axial position. The projections of each frame onto these principal components (PC scores) can be plotted against one another (see Fig. 3d), featuring a clear trace associated with the axial motion. As explained in the Methods section, by parametrising and calibrating this score-space trajectory, we can work out the z position. The axial coordinate can be calibrated using the x and y trajectories via energy equipartition, since the Brownian motion of the trapped particle is isotropic at high frequencies, which are not affected by the optical trap. A typical particle trajectory is shown in Fig. 3e, where all three Cartesian coordinates are plotted against time. The corner frequencies of the trap can now be extracted from the power spectral densities, shown in Fig. 3f, and with knowledge of the particle size and the viscosity of medium the trap stiffness along each dimension can be estimated. Further details on the tracking procedure can be found in the Methods section.

Figure 4a-e summarises our study of the trap stiffness along each coordinate for varying fibre lengths. We used the same segment throughout the study, re-cleaving it several times to shorten its length in increments of 25 mm. To verify that the axial confinement is indeed due to optical forces, the fibre was oriented horizontally so as to eliminate the gravitational effects in the axial direction. The trapped objects were silica microspheres of 1.5 μm in diameter and the wavelength was 1064 nm. Increasing the fibre length clearly degrades the trap stiffness, particularly in the axial direction. At the same time, we see that the power dependence also visibly departs from linearity, especially for longer fibres. Both these effects are connected to MDL. Even with MDL compensation the available NA is reduced (as shown in 2), moreover for larger fibres the MDL compensation intensifies the power of the lossy modegroups, which leads to temperature increase due to optical absorption. This causes changes to the TM and consequently reduces quality of the optical traps. Comparing these results with the state-of-art HOT systems based on high-NA microscope objectives, our traps are roughly one order of magnitude weaker. This is in good agreement with our expectations – the optical traps only carry about 33% of the output optical power (see Supplementary Results 3 for more details) and, although sufficient for 3-D confinement, the available NA is $\approx 20-30\%$ lower.

Next to sufficiently strong confinement, practical applications of HOT also require fine positioning with nanometric precision, which may appear to be inconsistent with our construction of the TM from output modes organised in an orthogonal grid spaced by ≈0.23 μm. This problem may be resolved by realising that any diffraction-limited focus at an arbitrary position on the distal fibre endface can be also expressed as a linear superposition of the distal FPs. For instance, by weighting the relative amplitudes of two neighbouring FPs, we can relocate an optical trap anywhere between them (see Supplementary Results 4 for more details). Such a restriction does not apply to axial positioning since this

is achieved by adding an arbitrarily small amount of defocus to the proximal far-field, as explained earlier. In order to demonstrate fine positioning, we have implemented these principles to relocate an optical trap in a step-wise manner, both axially and laterally, while recording the particle position. Figure 4g-i reveals that even 5 nm lateral steps ($\approx 50\times$ smaller than the separation of the output modes) can still be resolved. Due to weaker localisation in the z-direction, the smallest resolvable axial steps are five times larger (Fig. 4k,l).

Both these studies clearly confirm that the trapping performance is indeed sufficient even for advanced applications in biomedical research [7, 48].

Discussion

To the best of our knowledge, this work is the first demonstration of three-dimensional holographic optical manipulation of micro-objects via a single-core optical fibre. In order to allow for this we have introduced a new class of all-solid step-index multimode fibres, which feature a previously unattainable level of NA, exceeding the value of 0.8, necessary for stable optical confinement of silica particles. Further we have introduced novel holographic algorithms that, by taking the mode-dependent loss into account, enable harnessing the available NA almost completely. Moreover our novel approaches enable positioning of multiple foci independently of one another, with nanometric precision in all three dimensions. The combination of novel fibres and the empowered algorithms therefore significantly enhanced our ability to deliver tightly focussed laser beams into difficult-to-access locations.

The versatility of the new instrument is demonstrated by simultaneous and dynamic 3-D manipulation of large assemblies of dielectric microparticles. The instrument's footprint can be as small as 35 µm in diameter, allowing us to demonstrate the manipulation of micro-objects within a turbid cavity, inaccessible to bulk optics. Quantitative analyses reveal that the performance of the fibre-based trapping system is not significantly lower than standard geometries of optical tweezers relying on bulk objective lenses. Particle confinement strength and fine positioning control are both well maintained, which suggest that the system is applicable without severe compromises. Other possible concerns might relate to the influence of fibre bending on the quality of resulting optical traps. A phenomenological demonstration of this effect, found in Supplementary Results 5 (see also Supplementary Media SM5), suggests that the resilience of the fibres is sufficient for a wide spectrum of practical applications, including *in vivo* experiments. Furthermore, it has been recently demonstrated that such deformations can be corrected for based on numerical modelling of light propagation through multimode fibres [35]. This same study also suggests that highly precise numerical modelling can substitute the process of TM acquisition, which can significantly simplify the currently complex experimental methods.

The work opens up new perspectives for the first applications of HOT inside complex environments, excitingly including *in-vivo* studies. Manipulating optical traps in three dimensions is a vitally important attribute in such applications, because alternative means of mutually positioning the optical traps with respect to the sample (e.g. by the piezo-actuated stages commonly used *in vitro*) will no longer be feasible.

Finally, the work is broadly relevant beyond the applications of HOT, unlocking many new possibilities for modern biomedical research, where current approaches frequently rely on tight focussing of laser light. This work also provides a direct route to implementation of highly advanced imaging techniques and microscopy deep inside living tissues, which due to their optically turbid nature are currently inaccessible for bulk optics.

In the future, we plan to explore the use of light signals reflected back along the MMF both to image the sample and to provide a means of particle tracking, thus eliminating the need for external imaging of the sample.

References

[1] Ashkin, A., Dziedzic, J. M., Bjorkholm, J. E. & Chu, S. Observation of a single-beam gradient force optical trap for dielectric particles. *Opt. Lett.* **11**, 288–290 (1986).

[2] Fazal, F. M. & Block, S. M. Optical tweezers study life under tension. *Nat. Photonics* **5**, 318–321 (2011).

[3] Svoboda, K. & Block, S. M. Force and velocity measured for single kinesin molecules. *Cell* **77**, 773–784 (1994).

[4] Bustamante, C., Macosko, J. C. & Wuite, G. J. L. Grabbing the cat by the tail: Manipulating molecules one by one. *Nat. Rev. Mol. Cell Biol.* **1**, 130–136 (2000).

[5] Bustamante, C., Bryant, Z. & Smith, S. B. Ten years of tension: single-molecule DNA mechanics. *Nature* **421**, 423–427 (2003).

[6] Grier, D. G. A revolution in optical manipulation. *Nature* **424**, 810–816 (2003).

[7] Dholakia, K. & Reece, P. Optical micromanipulation takes hold. *Nano Today* **1**, 18–27 (2006).

[8] Padgett, M. & Di Leonardo, R. Holographic optical tweezers and their relevance to lab on chip devices. *Lab Chip* **11**, 1196–1205 (2011).

[9] Denk, W., Strickler, J. & Webb, W. Two-photon laser scanning fluorescence microscopy. *Science* **248**, 73–76 (1990).

[10] Hell, S. W. & Wichmann, J. Breaking the diffraction resolution limit by stimulated emission: stimulated-emission-depletion fluorescence microscopy. *Opt. Lett.* **19**, 780–782 (1994).

[11] Dickson, R. M., Cubitt, A. B., Tsien, R. Y. & Moerner, W. E. On/off blinking and switching behaviour of single molecules of green fluorescent protein. *Nature* **388**, 355–358 (1997).

[12] Betzig, E. *et al.* Imaging intracellular fluorescent proteins at nanometer resolution. *Science* **313**, 1642–1645 (2006).

[13] Jun, Y., Tripathy, S. K., Narayanareddy, B. R., Mattson-Hoss, M. K. & Gross, S. P. Calibration of optical tweezers for in vivo force measurements: How do different approaches compare? *Biophys. J.* **107**, 1474–1484 (2014).

[14] Zhong, M.-C., Wei, X.-B., Zhou, J.-H., Wang, Z.-Q. & Li, Y.-M. Trapping red blood cells in living animals using optical tweezers. *Nat. Commun.* **4**, 1768 (2013).

[15] Bambardekar, K., Clément, R., Blanc, O., Chardès, C. & Lenne, P.-F. Direct laser manipulation reveals the mechanics of cell contacts in vivo. *Proc. Natl. Acad. Sci.* **112**, 1416–1421 (2015).

[16] Constable, A., Kim, J., Mervis, J., Zarinetchi, F. & Prentiss, M. Demonstration of a fiber-optical light-force trap. *Opt. Lett.* **18**, 1867–1869 (1993).

[17] Ribeiro, R. S. R., Soppera, O., Oliva, A. G., Guerreiro, A. & Jorge, P. A. S. New trends on optical fiber tweezers. *J. Light. Technol.* **33**, 3394–3405 (2015).

[18] Liberale, C. *et al.* Miniaturized all-fibre probe for three-dimensional optical trapping and manipulation. *Nat. Photonics* **1**, 723–727 (2007).

[19] Berthelot, J. *et al.* Three-dimensional manipulation with scanning near-field optical nanotweezers. *Nat. Nanotechnol.* **9**, 295–299 (2014).

[20] Guck, J., Ananthakrishnan, R., Moon, T. J., Cunningham, C. C. & Käs, J. Optical Deformability of Soft Biological Dielectrics. *Phys. Rev. Lett.* **84**, 5451–5454 (2000).

[21] Guck, J. *et al.* Optical deformability as an inherent cell marker for testing malignant transformation and metastatic competence. *Biophys. J.* **88**, 3689–3698 (2005).

[22] Kreysing, M. K. *et al.* The optical cell rotator. *Opt. Express* **16**, 16984 (2008).

[23] Kreysing, M. *et al.* Dynamic operation of optical fibres beyond the single-mode regime facilitates the orientation of biological cells. *Nat. Commun.* **5**, 5481 (2014).

[24] Mosk, A. P., Lagendijk, A., Lerosey, G. & Fink, M. Controlling waves in space and time for imaging and focusing in complex media. *Nat. Photonics* **6**, 283–292 (2012).

[25] Vellekoop, I. M. & Mosk, A. P. Focusing coherent light through opaque strongly scattering media. *Opt. Lett.* **32**, 2309–2311 (2007).

[26] Bertolotti, J. *et al.* Non-invasive imaging through opaque scattering layers. *Nature* **491**, 232–234 (2012).

[27] Čižmár, T., Mazilu, M. & Dholakia, K. In situ wavefront correction and its application to micromanipulation. *Nat. Photonics* **4**, 388–394 (2010).

[28] Di Leonardo, R. & Bianchi, S. Hologram transmission through multi-mode optical fibers. *Opt. Express* **19**, 247–254 (2011).

[29] Čižmár, T. & Dholakia, K. Shaping the light transmission through a multimode optical fibre: complex transformation analysis and applications in biophotonics. *Opt. Express* **19**, 18871–18884 (2011).

[30] Bianchi, S. & Di Leonardo, R. A multi-mode fiber probe for holographic micromanipulation and microscopy. *Lab Chip* **12**, 635–639 (2012).

[31] Čižmár, T. & Dholakia, K. Exploiting multimode waveguides for pure fibre-based imaging. *Nat. Commun.* **3**, 1027 (2012).

[32] Choi, Y. *et al.* Scanner-free and wide-field endoscopic imaging by using a single multimode optical fiber. *Phys. Rev. Lett.* **109**, 203901 (2012).

[33] Papadopoulos, I. N., Farahi, S., Moser, C. & Psaltis, D. High-resolution, lensless endoscope based on digital scanning through a multimode optical fiber. *Biomed. Opt. Express* **4**, 260–270 (2013).

[34] Papadopoulos, I. N., Farahi, S., Moser, C. & Psaltis, D. Focusing and scanning light through a multimode optical fiber using digital phase conjugation. *Opt. Express* **20**, 10583 (2012).

[35] Plöschner, M., Tyc, T. & Čižmár, T. Seeing through chaos in multimode fibres. *Nat. Photonics* **9**, 529–535 (2015).

[36] Morales-Delgado, E. E., Psaltis, D. & Moser, C. Two-photon imaging through a multimode fiber. *Opt. Express* **23**, 32158 (2015).

[37] Plöschner, M. *et al.* Multimode fibre: Light-sheet microscopy at the tip of a needle. *Sci. Rep.* **5**, 18050 (2015).

[38] Amitonova, L. V. *et al.* High-resolution wavefront shaping with a photonic crystal fiber for multimode fiber imaging. *Opt. Lett.* **41**, 497 (2016).

[39] Papadopoulos, I. N., Farahi, S., Moser, C. & Psaltis, D. Increasing the imaging capabilities of multimode fibers by exploiting the properties of highly scattering media. *Opt. Lett.* **38**, 2776–2778 (2013).

[40] Choi, Y., Yoon, C., Kim, M., Yang, J. & Choi, W. Disorder-mediated enhancement of fiber numerical aperture. *Opt. Lett.* **38**, 2253–2255 (2013).

[41] Bianchi, S. *et al.* Focusing and imaging with increased numerical apertures through multimode fibers with micro-fabricated optics. *Opt. Lett.* **38**, 4935–4937 (2013).

[42] Wadsworth, W. J. *et al.* Very high numerical aperture fibers. *IEEE Photonics Technol. Lett.* **16**, 843–845 (2004).

[43] Popoff, S. M. *et al.* Measuring the transmission matrix in optics: An approach to the study and control of light propagation in disordered media. *Phys. Rev. Lett.* **104**, 100601 (2010).

[44] Popoff, S. M., Lerosey, G., Fink, M., Boccara, A. C. & Gigan, S. Image transmission through an opaque material. *Nat. Commun.* **1**, 1–5 (2010).

[45] Gloge, D. Weakly guiding fibers. *Appl. Opt.* **10**, 2252–2258 (1971).

[46] Issa, N. A. High numerical aperture in multimode microstructured optical fibers. *Appl. Opt.* **43**, 6191–6197 (2004).

[47] Ho, K.-P. & Kahn, J. M. Mode-dependent loss and gain: statistics and effect on mode-division multiplexing. *Opt. Express* **19**, 16612–16635 (2011).

[48] Neuman, K. C. & Block, S. M. Optical trapping. *Rev. Sci. Instrum.* **75**, 2787–2809 (2004).

[49] Jiang, X. *et al.* Single-mode hollow-core photonic crystal fiber made from soft glass. *Opt. Express* **19**, 15438–15444 (2011).

[50] Jiang, X. *et al.* Supercontinuum generation in ZBLAN glass photonic crystal fiber with six nanobore cores. *Opt. Lett.* **41**, 4245–4248 (2016).

[51] `https://drive.google.com/file/d/0B_j9JcELW7ldVmRXeEoyOXhWOEU/view`.

[52] Richards, B. & Wolf, E. Electromagnetic diffraction in optical systems. II. Structure of the image field in an aplanatic system. *Proc. R. Soc. A Math. Phys. Eng. Sci.* **253**, 358–379 (1959).

[53] Novotny, L. & Hecht, B. *Principles of Nano-Optics* (Cambridge University Press, Cambridge, 2006).

[54] Kramers, H. Brownian motion in a field of force and the diffusion model of chemical reactions. *Physica* **7**, 284–304 (1940).

Acknowledgements

I.T.L. and S.T. acknowledge funding from the People Programme (Marie Curie Actions) of European Union's Seventh Framework Programme (FP7/2007-2013) under REA grant agreement n^o 608144. I.T.L. also acknowledges the financial support of the EU, the "Thüringer Ministerium für Wirtschaft, Wissenschaft und Digitale Gesellschaft", the "Thüringer Aufbaubank" and the Federal Ministry of Education and Research, Germany (BMBF). M.Š. and T.Č. acknowledge support from the European Regional Development Fund through project n^o CZ.02.1.01/0.0/0.0/15_003/0000476. T.Č. acknowledges also the University of Dundee and SUPA – Scottish Universities Physics Alliance (PaLS initiative) for financial support. X.J. and P.St.J.R. thank Mr. Fehim Babic for his assistance in drawing the fibres. The authors also thank Dr. Keith Wilcox and Elliot Scientific Ltd. for lending equipment used in the experiments.

Author contributions

I.T.L. and S.T. and T.Č performed all experiments. X.J. and P.St.J.R. designed and manufactured the optical fibres. M.Š modelled the optical tweezers. I.T.L., A.C, and T.Č. analysed the results. T.Č. led the project. I.T.L. and T.Č. wrote the manuscript with contributions from all authors.

Materials & Correspondence

Correspondence and requests for materials should be addressed to T.Č.

Competing financial interests

The authors declare no competing financial interests.

Methods

Fibre fabrication

The step-index lead-silicate fibre had core and cladding formed from Schott SF57 and LLF1 glass respectively, with refractive indices 1.8117 and 1.5346 at 1.064 µm, resulting in an NA of 0.96. The glass transformation temperatures (T_g, corresponding to a viscosity of $\sim 10^{12}$ Pa s) are 414 °C for SF57 and 431 °C for LLF1, and for successful fibre drawing it is crucial that the furnace temperature is chosen such that the viscosity of the "harder" cladding glass lies in the range 10^5 Pa s to 10^6 Pa s. The fibre preform was prepared by a multi-step rod-in-tube process, and the fibre was drawn at ∼725 °C, corresponding to the viscosity of $10^{5.7}$ Pa s for the LLF1 glass, and $10^{3.4}$ Pa s for the SF57 glass. The fibre drawing was carried out following the procedure developed for photonic crystal fibres [49, 50], including a custom-designed heating element to provide a highly uniform temperature distribution around the preform. During drawing, the endface of the preform was connected to a vacuum pump so as to close the gaps between the rod and jacket tube. An outer UV-cured polymer coating increases the mechanical robustness of the fibre. Supplementary Figure S9a shows a scanning electron micrograph (SEM) of the final fibre structure.

In order to reduce the lateral instrument footprint, the fibres are post-processed into a flat-cone termination, as shown in Supplementary Figure S9b, where the cladding thickness was reduced from 125 µm down to 35 µm at the tip. The fibres are held by a fibre clamp (Thorlabs SM1F1-250) fixed onto a stepper motor allowing for rotation (∼ 5 rpm) around their axis. An xy translation mount (Thorlabs CXY1) is used for the fine adjustment to correct for eccentricity in the rotation. A fibre polishing sheet (Thorlabs LF3D) has been cut into the shape of a circle with a diameter of 4 cm and fixed onto a fast-rotating stage (∼ 500 rpm). The sheet is then brought into contact with the fibre at a grazing angle (∼ 5°) to polish out the cladding. A low-magnification microscope objective together with a tube lens and a CCD camera are used to monitor the fibre post-processing.

Optical trapping procedures

The optical trapping experiments start with placing a fibre segment into the optical pathway, which is detailed in Supplementary Figure S1. The first diffraction order signal of holographically modulated laser light is isolated in the proximal far-field plane and relayed through an oil-immersion medium into the proximal end of the fibre. A water-filled custom-made cuvette composed from 170 µm thick coverslips (inset of Supplementary Figure S1) is mounted in the system to immerse the distal end into the liquid. A water-immersion microscope objective lens is translated towards the cuvette from the opposite side with water-index-matching medium being applied in-between the cuvette-objective interface. The optical signal leaving the objective back aperture is further imaged on a CCD using a tube lens. With this configuration, we proceed to measure the MDL and TM [35], which provides the basis for all necessary holographic modulations (see Supplementary Methods 2 for details). A suspension of silica microspheres (Duke Standards^{TM} with 1.57 µm±0.02 µm in diameter) is pipetted into the cuvette and let diffuse within the water medium. For the following procedures we block the trapping wavelength using a dielectric short-pass filter and provide incoherent illumination of the sample by using an LED at a visible wavelength. For the *en face* view, the illumination signal is delivered through the high-NA fibre (and the proximal objective), whereas for the side-view a stand-alone Köhler illumination pathway is provided. In all cases when the side-view imaging pathway is used, the water illumination objective is displaced away from the cuvette to allow sufficient space for the side-view imaging lens. A single optical trap or an assembly of traps is generated via computer-controlled SLM modulation which, based on the *en face* view or side-view camera-feedback, is permanently adjusted manually from a LabView-based interface in order to confine the corresponding amount of particles diffusing into the vicinity of the distal end of the high-NA fibre. Records of the confined particles are then used for demonstrations of the instrument's versatility (Fig. 2, see also Supplementary Media SM1-SM5) or characterisation of the optical traps (Figs. 3 and 4). To demonstrate holographic manipulation within complex environments (Fig. 2c) the semi-opaque cavity is mounted on a lateral wall of the custom-made cuvette. The cuvette containing the cavity is then manipulated with respect to the distal fibre end by a manual 3-D positioning stage.

Particle tracking

Records of a confined particle are obtained with the *en face* imaging pathway at the frame-rate of 1 kHz and pixel resolution of 200×40. For each record of the trapped particle we also provide a background record (with no particles in the field of view), whose time-averaged signal is then subtracted from each frame of the particle record in order to eliminate effects originating from non-uniformities in the illumination signal. The pixel size is 7.4 µm and the magnification of the *en face* imaging pathway is 66×. The Matlab code, which has been used to analyse the records, can be found at [51]. A time-averaged frame of the whole record is used to determine the approximate position of the particle, and the whole record is cropped to a size of 32×32 pixels around the particle's image. Each frame of the record is then subjected to an optimisation procedure where the shift-property of Fourier transform is employed: the 1-D Fourier transform of each row of the image data is calculated, which is multiplied by a phase term of $\exp(2\pi i \vec{x} d_x/N)$, where d_x is the horizontal shift to be applied in units of pixels, $\vec{x}$ is a vector of pixel indices $(-N/2,\ -N/2+1,\ ...,\ -1,\ 0,\ 1,\ ...,\ N/2-2,\ N/2-1)$, and N is the size of the vector ($N = 32$). The inverse Fourier transform is calculated from the result to obtain each row of the spatially shifted frame. The optimisation procedure varies the amount of d_x in order to obtain a frame that gives the minimum difference (least-squares sum) from its mirror image. The value of d_x maximising the mirror symmetry of the image gives the x-coordinate of the particle for the actual frame in units of pixels size. The same procedure is then applied to each column of the image to symmetrise the frame vertically and obtain the y-coordinate. Alternatively, the optimisation procedure could search for both coordinates simultaneously using a 2-D Fourier transform, but this has been found to be significantly slower. All symmetrised frames are then reshaped into a vector of $1 \times N^2$ and placed into columns of a 2-D matrix containing the whole record. The Matlab inbuilt principal component analysis ('pca' command) is used to calculate the principal component vectors (those reshaped back into 32×32 pixels are shown in Fig. 3c) and the score for each frame. The scores of the first two principal components form a clear z-trajectory in the 2-D PC space (Fig. 3d), where each frame of the record is represented as a single point.

The first step in the parametrisation of the trajectory is searching for the 'origin' point featuring the highest concentration of the score-points in PC space. In the second step, we search for a circular (soft-apertured) subspace, whose centre is displaced from the 'origin' point by a fixed (very small) distance and also features the highest concentration of score-points from all such sub-spaces at the fixed radius from the 'origin'. This provides the tangential vector to the z-trajectory. Then we sequentially translate the 'origin' point in small increments along the tangential vector, with each step including a correction to the tangential vector. Because the optimisation function, searching for the optimal angle of the tangential vector, has two local maxima for two opposite angles (corresponding to forward and backward displacement), a weighting term providing preferential movement in the forward direction (with respect to the previous iteration) has been included to prevent reversing the motion and cycling. This way, we follow in small increments until we reach the place where the concentration of particles is below a certain threshold. When we reach one end of the trajectory, we reverse the tangential vector and sequentially move the 'origin' point backwards, while keeping record of its actual position in the PC space.

Further, we extrapolate each end of the obtained z-trajectory beyond the location of the score-points and re-sample it so the distance between neighbouring points is significantly smaller when compared to the expected inaccuracy, which can be estimated from the outer spread (thickness) of the score-point cloud from the z-trajectory. The equidistant z-trajectory is shown as a red line in (Fig. 3d). Finally, for each score-point (representing a frame of the record) we find the closest point of the reconstructed z-trajectory, whose index is associated with the uncalibrated z-coordinate.

Although it is very reasonable to assume that the z-motion of the particle results in a monotonous response in PC space (moving along a 1-D trajectory), there is no indication that such response shall be linear. Within our experiments, the non-linear behaviour has however only been significant in cases where the particle was confined at very low optical powers. As shown in Supplementary Fig. S10, which has been obtained for the output power of 2.2 mW, this nonlinearity can be easily characterised by grouping the data into sub-intervals, calculating the standard deviation for each of them and applying a polynomial fit, which then serves as the basis for correction to the z-trajectory.

While the x and y coordinates can be calibrated from the known pixel size and the magnification of the used imaging pathway, the linearised z trajectory can be calibrated by assuming that the Brownian motion at high frequencies is not affected by the trap and therefore remains isotropic along all Cartesian coordinates.

Estimation of the optical trap stiffness

The power spectrum density (PSD) of particle trajectories are used in the assessment of the trap stiffness [48]. The power spectra are calculated as the squared absolute value of the Fourier transform for each trajectory, which is further fitted by a Lorentzian function:

$$\mathrm{PSD} = \frac{a}{f^2 + f_c^2},$$

where f is the frequency coordinate of the Fourier spectrum and a and f_c are parameters of the fit. The optical stiffness κ can be recovered from the corner frequency parameter f_c as:

$$\kappa = 2\pi\beta f_c,$$

where the hydrodynamic drag

$$\beta = \frac{6\pi\nu a}{1 - \frac{9}{16}\frac{a}{h} + \frac{1}{8}\left(\frac{a}{h}\right)^3 - \frac{45}{256}\left(\frac{a}{h}\right)^4 - \frac{1}{16}\left(\frac{a}{h}\right)^5}$$

already includes Faxen's law correction, ν is the viscosity of the medium, a is the radius of the particle and h is the distance of the particles centre from the fibre facet. Throughout our analyses of the optical stiffnesses, we have confined the particles at a distance of $\approx$5 µm away from the fibre. This value has been used as the estimate of the particle displacement from the fibre facet. We note that increasing power causes further axial relocation of the trap away from the fibre, as shown in Supplementary Figure S8c. We have not corrected the hydrodynamic drag constant β for this effect as even in the most affected cases the imprecision in the estimate of h only brings a small inaccuracy to the resulting stiffness values (up to 5%).